Research Square

Preprints are preliminary reports that have not undergone peer review.
They should not be considered conclusive, used to inform clinical practice,
or referenced by the media as validated information.

Adsorption and photo-Fenton catalytic degradation of Orange II dye over cobalt ferrite nanoparticles and almond shell biochar

Martina Lorente
Universidad de Buenos Aires
Inés Salvador
Universidad de Buenos Aires
Ana Beatriz Fossati
afossati@fi.uba.ar

Universidad de Buenos Aires
Analía Verónica Russo
Universidad de Buenos Aires

Research Article

Keywords: almond shell biochar, azo dye degradation, cobalt ferrite, photo-Fenton process

Posted Date: September 11th, 2026

DOI: https://doi.org/10.21203/rs.3.rs-10885256/v1

License: This work is licensed under a Creative Commons Attribution 4.0 International License.
Read Full License

Additional Declarations: No competing interests reported.

Version of Record: A version of this preprint was published at Nanotechnology for Environmental Engineering on November 4th, 2026. See the published version at https://doi.org/10.1007/s41204-026-00623-z.

ADSORPTION AND PHOTO-FENTON CATALYTIC DEGRADATION OF ORANGE II DYE OVER COBALT FERRITE NANOPARTICLES AND ALMOND SHELL BIOCHAR

ABSTRACT

The purpose of this work is to synthesize and characterize new materials based on magnetic nanoparticles and almond shell biochar, and to evaluate their ability to remove Orange II dye from water sources. For this purpose, different systems were prepared: magnetic cobalt ferrite nanoparticles (MNP), MNP synthesized on almond shell biochar (BMNP) and a mechanical mixture of MNP and biochar (MM). These systems were characterized by X-ray diffraction, scanning electron microscopy, magnetic measurements and Fourier transform infrared spectroscopy, revealing different structural properties for the three samples. The adsorption kinetic was studied and the equilibrium time tested in this study was 50 minutes. The photo-Fenton catalytic degradation of Orange II was studied. For MNP system, tests were performed under different conditions: varying concentration of catalyst and peroxide, and pH. The concentration of peroxide of 600 ppm, the catalyst concentration of 75 mg/l and pH 3 were the conditions that allowed obtaining higher degradation percentages (> 90%). Under these optimal operation conditions, the dye removal capacity was evaluated for the three systems. BMNP system showed a higher degradation capacity (>97%) in less time and more than 95 % of the sorption capacity remained after 5 successive sorption-washing cycles, suggesting an excellent reusability. These cobalt ferrite nanoparticles synthesized on biochar are presented as an efficient and reusable catalyst to remove dyes like Orange II from wastewater from the textile and food industries using solar energy.

Keywords: almond shell biochar, azo dye degradation, cobalt ferrite, photo-Fenton process

1. INTRODUCTION

Water pollution has become a major environmental concern directly compromising water security, aquatic biodiversity and public health [1]. While anthropogenic pollution sources are diverse – raging from urban and agrochemical drainage water to solid waste – the indiscriminate discharge of untreated industrial effluents remains one of the most severe agents of aquatic degradation [2, 3].

Among the complex spectrum of industrial pollutants, synthetic dyes are a major concern due to their massive production volume, geographic dispersion and high environmental persistence [4]. These compounds are engineered to resist light, washing and chemical degradation. This intrinsic structural stability severely restricts their natural biodegradation and drastically limits the efficiency of wastewater treatment plants based on conventional biological or physicochemical processes [5]. In particular, azo dyes represent the most prevalent and environmentally problematic class of industrial colorants, dominating more than 75 % of the global market for textile, leather and food applications [6, 7]. These dyes are characterized by one or more azo functional groups (-N=N-) that can act as the chromophores responsible for coloration. However, they also act as barriers to biodegradation and can generate mutagenic or carcinogenic intermediates. Consequently, Orange II is widely utilized as a model compound to represent this family, enabling the evaluation of both thermodynamic and kinetic performance of novel remediation systems [8].

Advanced oxidation processes (APOs) have emerged as highly promising alternatives for degrading these persistent synthetic pollutants [9]. These systems rely on the in situ generation of non-selective, highly reactive radical species (hydroxyl radicals, •OH) to oxidize organic compounds. These radicals possess an exceptionally high standard reduction potential (2.80 V vs. NHE) which enables them to non-selectively attack, fragment and mineralize complex organic molecules into simpler biodegradable by-products or, ideally, into carbon dioxide (CO_2) and water (H_2O) [10].

Fenton and photo-Fenton processes are widely recognized as two of the most effective AOPs due to their low-cost reagents and high kinetic efficiency. While conventional Fenton process relies on the catalytic decomposition of hydrogen peroxide (H_2O_2) by ferrous salts (Fe^{2+}) in an acidic medium [11], the photo-Fenton process drastically enhances this reaction by incorporating UV-visible light irradiation (solar or artificial). This light irradiation drives the photolysis of H_2O_2 (Eq. 1), accelerating the •OH radicals generation and promoting the reduction of Fe^{3+} to Fe^{2+} (Eq. 5), closing an efficient catalytic cycle [12]:

$$H_2O_2 + h\nu \rightarrow 2\ {\bullet}OH \qquad (Eq.1)$$

$${\bullet}OH + \text{dye} \rightarrow intermediates \qquad (Eq.2)$$

$${\bullet}OH + intermediates \rightarrow CO_2 + H_2O + mineralized\ products \qquad (Eq.3)$$

The enhanced performance of photo-Fenton process lies in its ability to overcome the rate-limiting step of the classical Fenton reaction through simultaneous photochemical pathways that maximize the production of $\bullet OH$ radicals via the following reactions:

$$Fe^{2+} + H_2O_2 \rightarrow Fe^{3+} + {\bullet}OH + OH^- \qquad (Eq.4)$$

$$Fe^{3+} + H_2O + h\nu \rightarrow {\bullet}OH + Fe^{2+} + H^+ \qquad (Eq.5)$$

In addition, Fe^{3+}-peroxy complexes formed by the photolysis of Fe^{3+} and H_2O_2 may directly attack the dye structure, thereby accelerating the discoloration of azo dyes [13]:

$$\text{dye} + Fe^{3+} \rightarrow Fe^{2+} + \text{dye}^+ \qquad (Eq.6)$$

$$\text{dye}^+ (\text{or dye}) + {\bullet}OH \rightarrow degradation\ products \qquad (Eq.7)$$

Despite these advantages, homogeneous photo-Fenton process faces several limitations including a narrow operating pH range, difficult catalyst recovery and potential iron leaching [14-16]. To overcome these limitations, heterogeneous catalysis using spinel-type ferrite nanoparticles have emerged as promising heterogeneous catalyst due to their high chemical stability and intrinsic ferromagnetic properties that enable recovery from treated effluents using an external magnetic field. Soufi et al. present a comprehensive review of various aspects related to the utilization of spinel ferrite and their composites in catalytic applications [17]. Khan et al. summarize the recent advancements in synthesis methods, modification and the application of ferrites as photocatalysts [18]. Following a literature review, Sayeh et al. concluded that spinel ferrite-based materials show excellent organic pollutant removal efficiency, representing a promising strategy for industrial-

scale wastewater treatment [19]. In particular, cobalt ferrite ($CoFe_2O_4$) stands out as a narrow band gap semiconductor, which facilitates its catalytic activation under the visible light spectrum [20-22].

To mitigate nanoparticle aggregation – which severely restricts active surface area – and enhance photocatalytic activity, supporting composite materials on carbonaceous matrices has emerged as a promising strategy [23-25]. Biochar is a low-cost, carbon-rich, porous material obtained through the pyrolysis of residual biomass under anoxic or hypoxic conditions [26]. This material possesses a high specific surface an abundance of oxygen-containing functional groups across its structure. These characteristics allow biochar to function as an efficient adsorbent, capturing molecules directly at its surface. These surface functional groups provide active anchoring sites that thermally stabilize and disperse ferrite nanoparticles preventing nanoparticle aggregation, preserving maximum reactive surface area during synthesis and operation. Biochar also serves as an electron sink, suppressing photogenerated electron-hole recombination and driving efficient charge transport to maximize overall pollutant degradation.

Despite these advantages, the performance of cobalt ferrite supported on almond shell biochar for photo-Fenton degradation remains unexplored. In order to resolve this issue, this study reports the synthesis, characterization and application of cobalt ferrite nanoparticles supported on almond shell biochar (BMNP) to remove Orange II dye from aqueous solutions. For comparative purposes, magnetic cobalt ferrite nanoparticles (MNP) and a mechanical mixture of almond shell biochar and MNP (MM) were also evaluated. Furthermore, operating parameters such as catalyst and peroxide concentration, and pH were optimized and the adsorption kinetics, photo-Fenton catalytic performance and catalyst reusability were investigated. This work highlights the potential of BMNP as a reusable catalyst to remove industrial dyes, such as Orange II, under solar irradiation.

2. EXPERIMENTAL

2.1Materials

All inorganic and organic chemicals used in this study were of analytical grade. Ferric nitrate nonahydrate ($Fe(NO_3)_3.9H_2O$), cobalt acetate tetrahydrate ($Co(CH_3CO_2)_2.4H_2O$), anhydrous citric acid ($C_6H_8O_7$), nitric acid (HNO_3), ammonia (NH_3), cobalt(II) chloride hexahydrate ($CoCl_2.6H_2O$), ferric chloride hexahydrate ($FeCl_3.6H_2O$), sodium hydroxide (NaOH), ethylene glycol ($HOCH_2CH_2OH$), sodium acetate trihydrate ($NaCH_3CO_2.3H_2O$), polyethylene glycol ($HO\text{-}(CH_2\text{-}CH_2\text{-}O\text{-})_n\text{-}H$), ammonium hydroxide ($NH_4OH$), hydrogen peroxide ($H_2O_2$). Dye solutions were prepared by dissolving Orange II ($C_{16}H_{11}N_2NaO_4$) in deionized water at 25 ºC (pH = 3.0 ± 0.1).

2.2Biochar preparation

Almond shell biochar was synthesized via pyrolysis according to the procedure described by Zabaleta et. al [27]. The raw almond shells were ground using a knife mill and sieve through a double-mesh stainless steel sieve with a 10 cm diameter to control particle size. The precursor was subjected to heat treatment in a programmable furnace at 500 ºC for 2 hours, using a heating rate of 10 ºC/min under an inert atmosphere.

2.3 Synthesis

2.3.1 Cobalt ferrite nanoparticles

For the synthesis of cobalt ferrite magnetic nanoparticles (MNP), a variation of a procedure reported by Sachse et al. was used [28]. The sample was prepared by the sol-gel method using ferric nitrate nanoaydrate and cobalt acetate tetrahydrate in a 2:1 Fe (III)/Co (II) molar ratio, followed by the addition of suitable amounts of anhydrous citric acid and nitric acid. The system was magnetically stirred, neutralized with ammonia and heated to 80 ºC. As the solution began to gel, ethylene glycol was added and heating was continued up to 160 ºC with manual stirring using a glass rod. Upon reaching the ignition temperature, the gel underwent auto-combustion, consuming the organic matter and leaving behind the precursor powder. Finally, the cobalt ferrite powder was obtained. Figure 1 shows the heterogeneous photo-Fenton degradation mechanism over MNP.

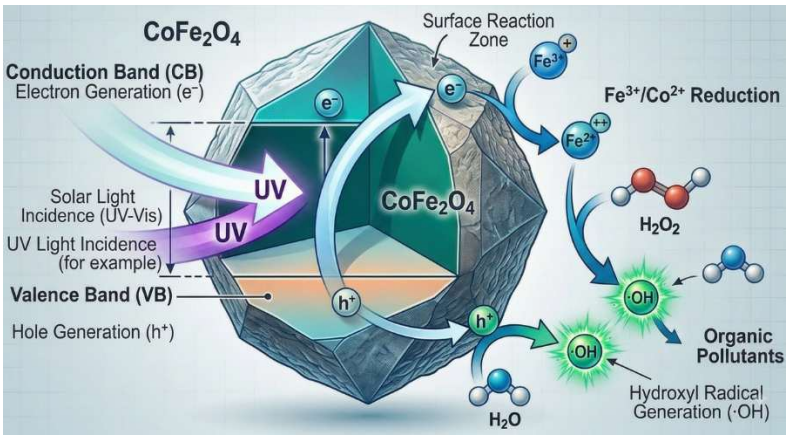


Figure 1. Schematic representation of the solar/UV activation mechanism of MNP and $\bullet OH$ radical generation. (Image generated using Gemini, based on prompts provided by the authors)

2.3.2 Cobalt ferrite nanoparticles synthesized on almond shell biochar

For the synthesis of cobalt ferrite nanoparticles on almond shell biochar (BMNP), the procedure reported by Wu et al. was applied with some modifications [29]. Two separate solutions were prepared (A and B). Solution A was obtained by dispersing almond shell biochar (prepared as described in Section 2.2) in distilled water under sonication at room temperature for 30 minutes. Solution B was prepared by dissolving ferric chloride hexaydrate and cobalt (II) chloride hexaydrate (Fe (III)/Co (II) molar ratio = 2:1) in distilled water, followed by sonication at 50 ºC for 30 minutes. Solution B was then added slowly to solution A. Subsequently, sodium hydroxide was added dropwise under continuous stirring until reaching a pH of 10. The resulting mixture was heated to 80 ºC for 45 minutes, centrifuged and washed with distilled water until neutral pH was reached. Finally, the product was dried in an oven at 80 ºC for 2 hours and calcined at 400 ºC using a heating rate of 10 ºC/min.

2.3.3 Mechanical mixture of nanoparticles and biochar

For the synthesis of the mixture of cobalt ferrite nanoparticles and almond shell biochar (MM), two solutions were prepared (A and B). Solution A was obtained by dispersing almond shell biochar (prepared as described

in Section 2.2) in distilled water under sonication for 30 minutes. Solution B was obtained by dispersing MNPs in distilled water under sonication for 30 minutes, maintaining the same ferrite/biochar ratio as in Section 2.3.2. Solution B was slowly added to solution A, and the pH was adjusted to 10 using ammonium hydroxide. The adjustment of the solution to pH 10 was carried out to modify the surface charge of both cobalt ferrite nanoparticles and almond shell biochar in order to promote particle dispersion, surface complexation and hydrogen bonding between the ferrite nanoparticles and the porous biochar [30]. The solution was then heated at 80 ºC for 45 minutes under mechanical stirring. Finally, the resulting mixture was centrifuged, washed with distilled water until a neutral pH was reached, and dried in a vacuum oven at 80 ºC.

Samples nomination is presented in Table 1.

Table 1. Samples nomination and description

Nomination	Description
MNP	Cobalt ferrite magnetic nanoparticles
BMNP	Cobalt ferrite magnetic nanoparticles synthetized on almond shell biochar
MM	Mechanical mixture of MNP and almond shell biochar

2.4 Characterization Techniques

The structural properties of the synthesized samples were analyzed by X-ray powder diffraction with a Rigaku SmartLab diffractometer using CuKα radiation in the range of 2θ from 20º to 80º. Field emission scanning electron microscope (FE-SEM, ZEIZZ ZUPRA 40) was used for morphological and ultrastructural analysis. Fourier Transform infrared (FTIR) spectra of the MNP, BMNP, and MM powder samples were recorded on a Nicolet 510P spectrometer using potassium bromide (KBr) pellets. The magnetic properties of the composite powders were performed at room temperature using a vibrating sample magnetometer (VSM), Lakeshore equipment, with an external field of up to 1.5 T.

2.5 Adsorption Experiments

Kinetic tests were performed to determine the equilibrium time for dye adsorption on the synthesized nanoparticle systems, establishing the baseline conditions required for subsequent photo-Fenton degradation. For this purpose, 45 mL of Orange II solution (40 mg/L) were placed in glass bottle flasks wrapped in aluminum foil. Then, 15 mg of nanoparticles were added and the system was continuously bubbled to ensure mixing. At specific time intervals, samples were collected, centrifuged for 1 minute and filtered to measure absorbance as a function of time with a Shimadzu Corporation UV-2401 Model Dual-Beam UV-Vis Spectrophotometer at 484 nm [31]. The amount of dye absorbed per unit mass of nanoparticles, Q_{ads} (mg/g), was calculated by Eq. 8:

$$Q_{ads} = \frac{(C_0 - C_t)v}{W} \qquad (Eq. 8)$$

where C_0 (mg/L) is the initial dye concentration (40 mg/L); C_t (mg/L) is the dye concentration at time t; v (L) is the sample volume (45 mL) and W (g) is the mass of adsorbent (0.015 g).

2.6 Photo-Fenton Degradation Experiments

To ensure effective dye degradation in wastewater treatment using the photo-Fenton process, the identification of optimal experimental conditions is essential. In this work, we investigate the influence of several parameters (dye, peroxide and catalyst concentrations, as well as pH) using MNPs as the catalyst.

The experimental setup used for these tests consists of a rectangular glass vessel coated on its four internal sides and inner base with aluminum foil. A Philips ML lamp (160 W, 220-230 V) was situated at a distance of 10 cm above the crystallizer containing the dye solution, catalyst and hydrogen peroxide. For all experiments, 100 mL of dye solution were used. Before initiating the experiment, the MNPs were sonicated for 2 hours to ensure adsorption equilibrium was reached. For photo-Fenton tests, the system was continuously bubbled and cooled with water to maintain a constant temperature of 20 ℃. Dye degradation was analyzed by Eq. 9:

$$D_{\%} = \frac{(C_0 - C_t)}{C_0} * 100\% \qquad (Eq. 9)$$

where C_0 is the initial dye concentration and C_t is the dye concentration at time t.

All kinetics and degradation experiments were duplicated to ensure reproducibility.

3. RESULTS AND DISCUSSION

3.1 Characterization

The comparative X-ray diffraction patterns of the four samples are shown in Figure 2 and demonstrate clear structural distinctions.

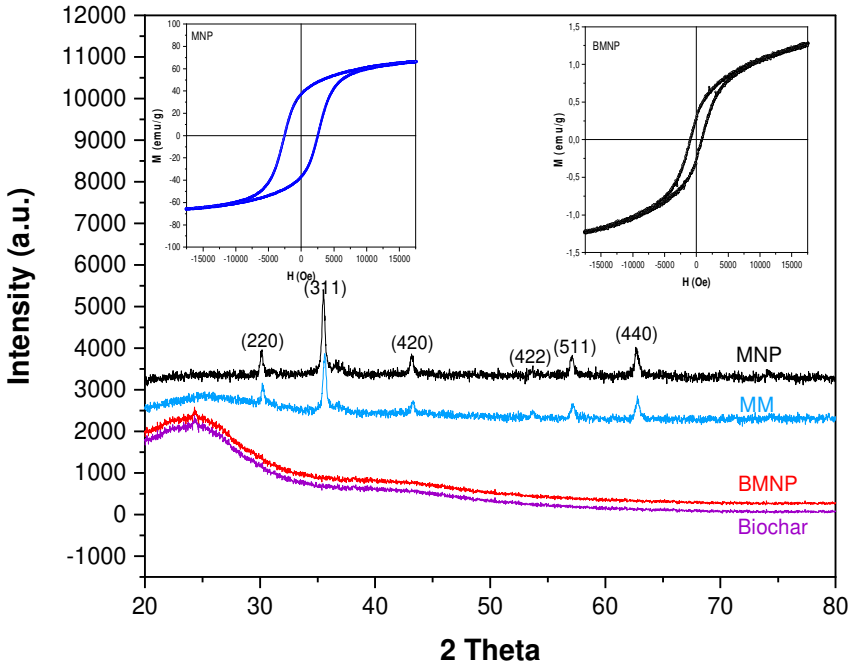


Figure 2. XRD diffraction patterns of biochar, MNP and the biochar-nanoparticle composites. Inset: Magnetic profiles of MNP (left) and BMNP (right)

The diffraction profile of the MNP sample displays characteristic peaks corresponding to cobalt ferrite [32], confirming a pure cubic spinel phase as the predominant crystalline structure. The crystalline size calculated from the XRD analysis is in the range of 10 nm. The XRD pattern of the biochar exhibits the typical broad peak associated with the carbonaceous structure of almond shells, attributed to the amorphous organic matter of cellulose, hemicellulose and lignin [33]. The diffraction profile of the BMNP exhibits the same broad peak as the biochar, indicating a higher proportion of this carbonaceous structured compared to the amount of cobalt ferrite of the sample. This indicates that the ferrite nanoparticles are highly dispersed, ultra-small or embedded within the porous framework of the biochar. The MM profile shows the diffraction peaks of the cubic spinel structure in addition to the broad peak associated with the carbonaceous structure of the biochar matrix, confirming the coexistence of both phases in the composite. Hence, the characterization results confirm the synthesis of cobalt ferrite nanoparticles and the carbon-ferrite composites.

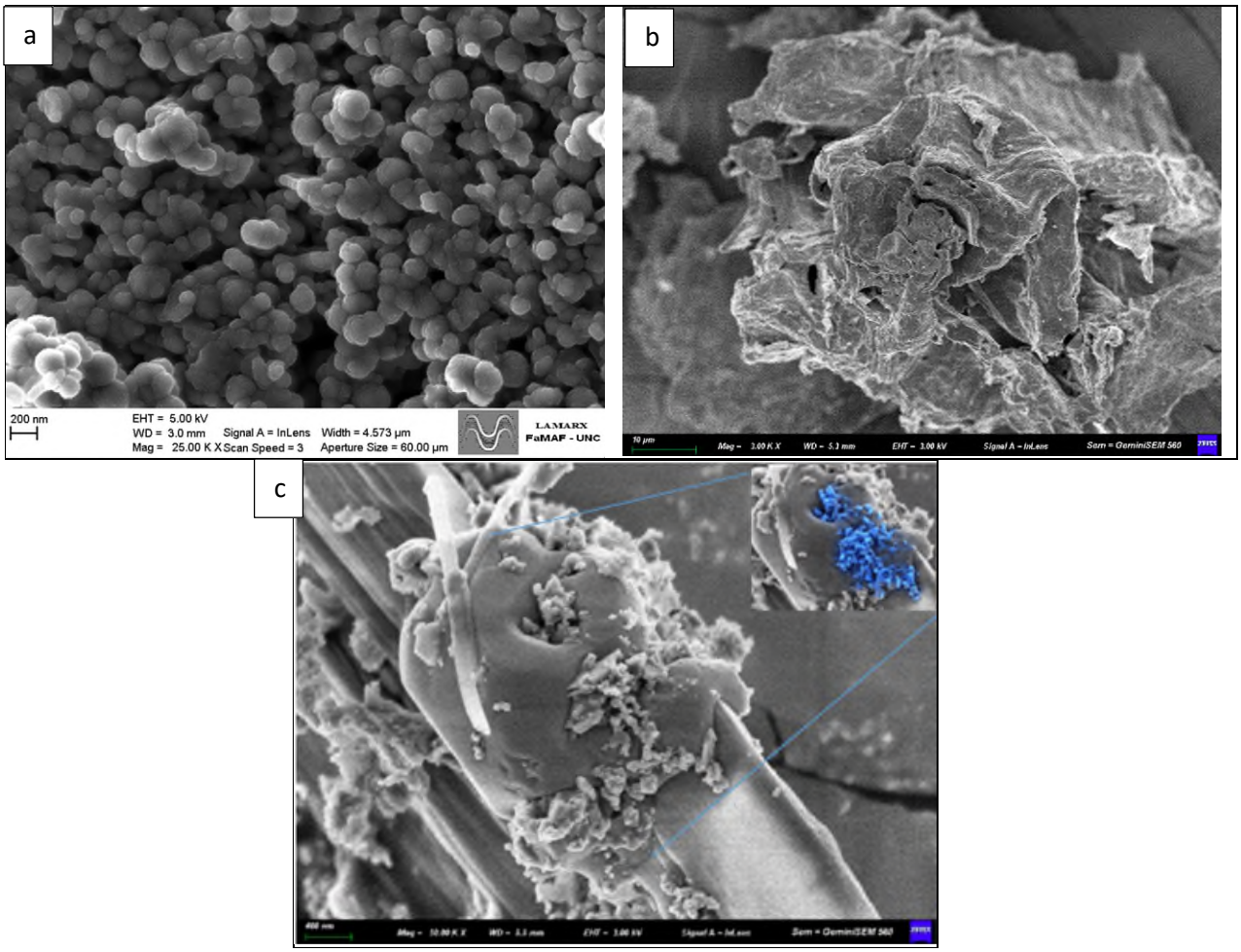


Figure 3. SEM images of: a) MNP, b) biochar and c) BMNP, Inset: magnified view of BMNP with the region containing nanoparticles highlighted in blue

Fig. 3.a shows spherical and homogeneously sized nanoparticles, with an average diameter of 70 nm. This size indicates particle agglomeration caused by their magnetic nature. Similar values have been reported in the literature [34, 35]. Fig. 3.b exhibits a laminar, fibrous structure characterized by irregular folds and fractures from lignocellulose carbonization [33]. This sheet-like morphology is typical of carbonaceous supports. Fig. 3.c presents the characteristic fibrous and laminar structure of the biochar. The nanoparticles are not only on the surface but also embedded within the folds of the biochar. In Fig. 3.c (inset) clusters of spherical particles are observed, highlighted in blue. They exhibit local agglomeration, characteristic of ferrite nanoparticles due to their magnetic interactions [36].

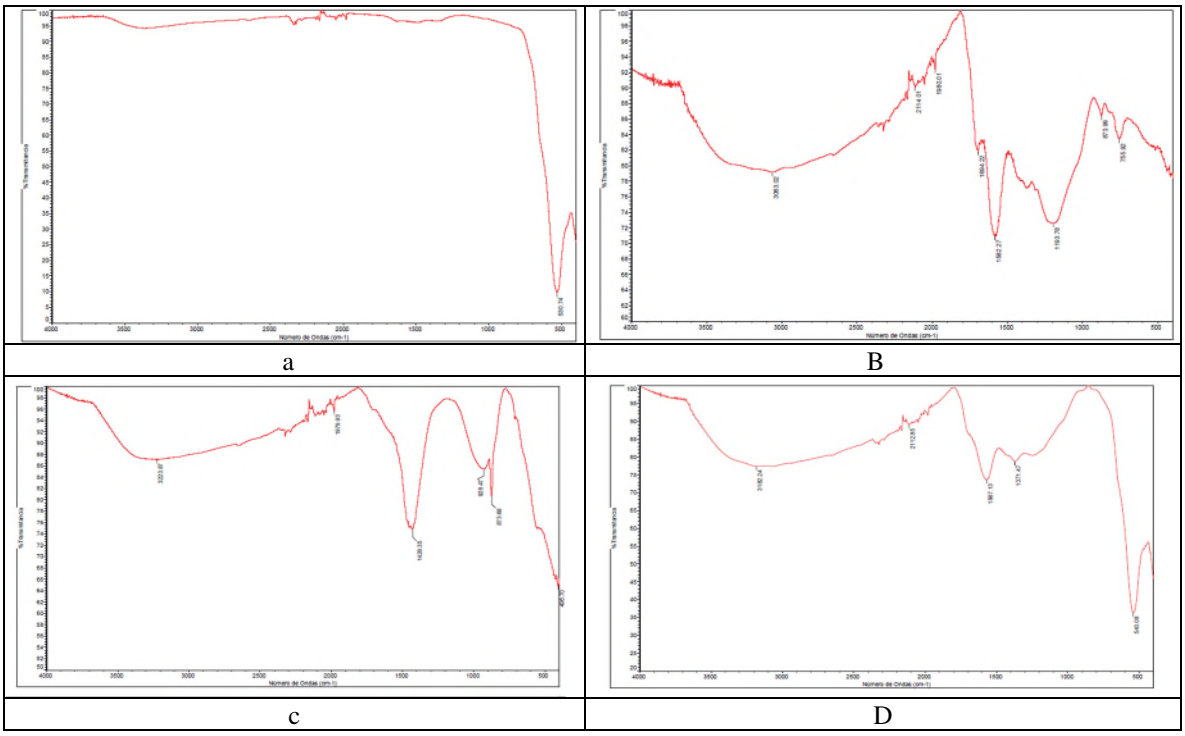


Figura 4. FTIR spectra: a) MNP, b) biochar, c) BMNP, d) MM

Figure 4 shows FT-IR spectra. Fig. 4.a: the band around 3400 cm^{-1} along with a minor peak near 1600 cm^{-1} corresponds to the O-H stretching and H-O-H bending from water adsorbed in the ferrite sample. The strong absorption peak at 570 cm^{-1} can be assigned to Co-O and Fe-O stretching bonds, characteristic of the spinel ferrite structure [37]. Fig. 4.b exhibits characteristic functional groups of lignocellulosic carbonized matter. The broad band at 3063 cm^{-1} is attributed to O-H stretching vibrations of hydroxyl functional groups and humidity. A peak at 1694 cm^{-1} indicates the C=O stretching of the carbonyl and carboxyl species from hemicellulose. The absorption band at 1582 cm^{-1} is assigned to the C=C aromatic ring stretching of the lignin, reflecting the successful carbonization of the precursor. The adsorption band at 1194 cm^{-1} is attributed to the C-O and C-O-C stretching vibrations of polysaccharides linkage. The peaks at 873 cm^{-1} and 775 cm^{-1} are characteristic of the out-of-plane C-H bending modes of aromatic rings within the biochar structure. This functional group assignment is consistent with reported FT-IR spectra of almond shell biochar [38]. The spectrum of the BMNP (Fig. 4.c) confirms the successful anchor of the cobalt ferrite nanoparticles onto the carbonaceous matrix. The broad absorption band at 3223 cm^{-1} is attributed to the O-H stretching vibrations of hydroxyl groups [39] and adsorbed water. The absorption band at 1428 cm^{-1} is assigned to the C=C aromatic ring stretching of the lignin, showing a subtle displacement compared to the biochar due to chemical interactions between the carbon surface and Co^{2+}/Fe^{3+}. The peaks at 928 cm^{-1} and 873 cm^{-1} are assigned to the out-of-plane C-H bending modes of the aromatic rings [38]. Figure 4.d presents the FTIR spectrum of the MM sample and confirms the co-existence of both component phases: MNP and biochar. The broad peak at 3300 cm^{-1} is assigned to O-H stretching vibrations of hydroxyl and phenolic functional groups [39] and humidity. The absorption band at 1700 cm^{-1} and 1600 cm^{-1} are attributed to the C=O stretching from carboxylic species from hemicellulose and C=C aromatic

ring stretching of the lignin respectively. The peak at 1400 cm^{-1} is assigned to C-H bending and the band at 1100 cm^{-1} corresponds to the C-O and C-O-C stretching vibrations of polysaccharides linkage. The strong signal at 570 cm^{-1} is assigned to the Co-O and Fe-O stretching vibrations [37], showing the effective integration of the spinel ferrite onto the biochar matrix.

The magnetic profiles of MNP and BMNP samples are exhibited in Figure 2 (Inset). The MNP magnetization curve (left) presents a ferromagnetic behavior with a high coercivity (Hc ~ 2500 Oe). The large coercive field confirms the strong magnetocrystalline anisotropy induced by Co^{2+} ions at the octahedral sites of the inverse spinel structure [40]. The saturation magnetization (Ms) and residual magnetization (Mr) obtained at room temperature were found to be ~ 67 emu/g and ~ 37 emu/g, respectively. The observed Ms value is lower than the theoretical bulk value for cobalt ferrite (~ 85 emu/g) which is attributed to surface spin-disorder, dead magnetic layers inherent to nanostructured materials [40]. The magnetization curve of BMNP (right) presents a significant decrease in total magnetization parameters compared to the curve of MNP. The Ms dropped from 67 (MNP) to 1.3 emu/g (BMNP) due to the high mass of the non-magnetic almond shell biochar in the composite acting as a magnetically inert matrix [41]. Despite the low magnetic saturation value, this magnetic response is more than adequate to achieve solid – liquid phase separation using a commercial magnet. The Hc decreased from ~ 2500 Oe for MNP to ~ 1000 Oe for BMNP. This reduction is commonly attributed to the porous almond shell biochar matrix, which disperses the nanoparticles and mitigates de interparticle magnetic dipole–dipole interactions reducing the coercivity compared to the pure sample (MNP).

The characterization techniques demonstrate the formation of three distinct materials with different structural, morphological and magnetic properties.

3.2 Batch adsorption kinetics

Figure 5 presents the time – dependent adsorption capacity of Orange II. The amount of dye adsorbed per unit mass of adsorbent (Q_{ads}) increases gradually with higher initial dye concentration until reaching a saturation value (Q_{max}). Adsorption equilibrium was reached at approximately 30 minutes for MNP (Q_{max} ~ 41 mg dye/ g adsorbent, Fig. 5.a), 60 minutes for biochar (Q_{max} ~ 50 mg dye/ g adsorbent, Fig. 5.b), 40 minutes for BMNP (Q_{max} ~ 44 mg dye/ g adsorbent, Fig. 5.c), and 50 minutes for MM (Q_{max} ~ 37 mg dye/ g adsorbent, Fig. 5.d). Adsorption equilibrium for the synthesized ferrites was established within 40 min. These results confirm that a contact time of 2 h is adequate to ensure complete adsorption–desorption equilibrium before starting photo-Fenton degradation tests.

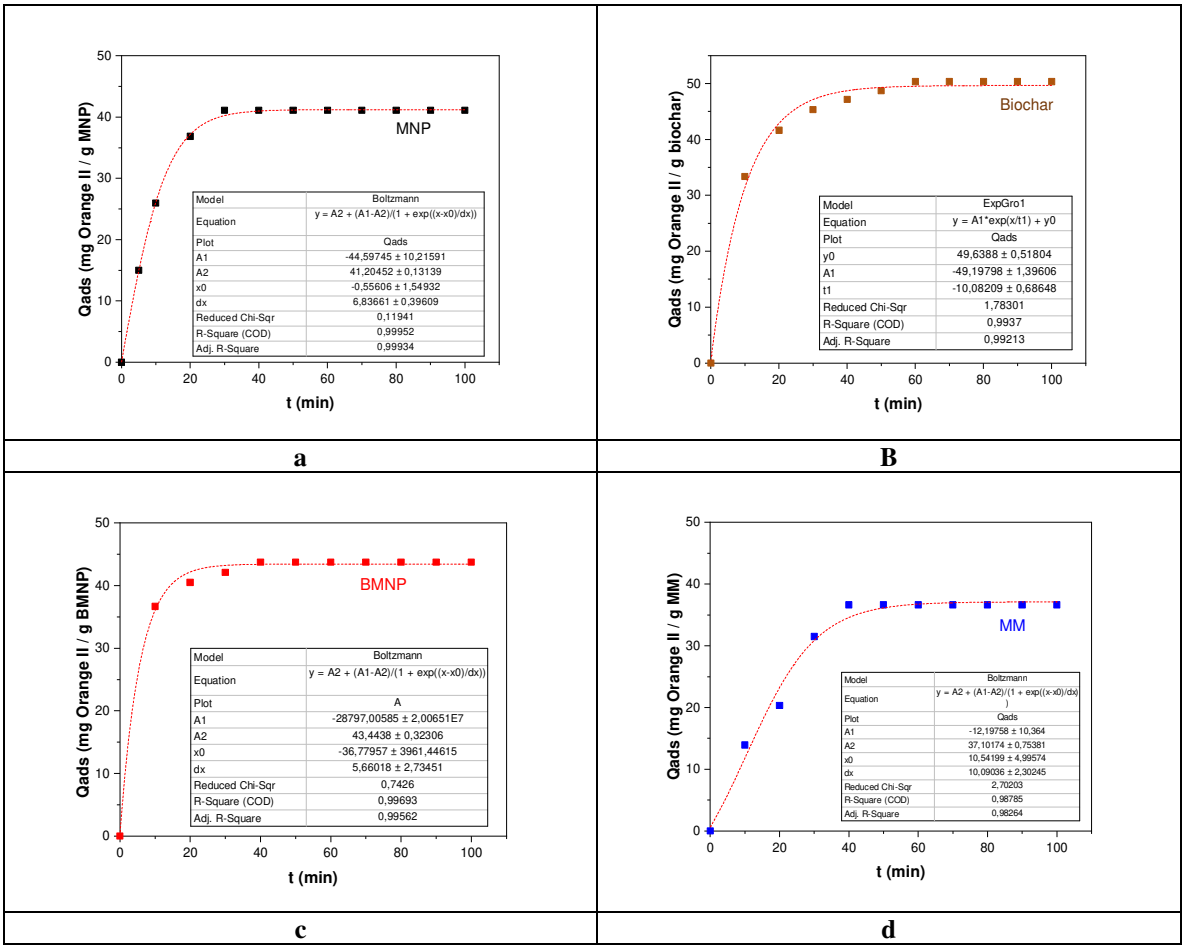


Figure 5. Effect of contact time on adsorption capacity of Orange II for the prepared samples: a) MNP, b) biochar, c) BMNP, d) MM

3.3 Photo-Fenton Degradation

3.3.1 Effect of dye concentration

The degradation efficiency of Orange II decreased as its initial concentration increased within the 10-60 mg/L range (Fig. 6.a). At 10 mg/L, the dye removal reached 98 % after 110 min. Under the same reaction time, the degradation efficiency decreased to 82%, 71% and 64% for initial concentrations of 20, 40 and 60 mg/L, respectively. Although the dye concentration increased, the generation rate of hydroxyl radicals (•OH) did not increase in the same proportion, resulting in a lower availability of hydroxyl radicals per unit of pollutant and reduced degradation efficiency. Furthermore, higher dye concentrations restrict light transmittance through the solution, reducing photon availability for radical generation. Consequently, the photo-Fenton process presents higher catalytic efficiency at lower dye concentrations [42, 43].

3.3.2 Effect of H_2O_2 dosage

Figure 6.b shows that Orange II degradation efficiency increased with higher concentrations of peroxide. At 90 min, dye degradation increased from 65% to 87% as the H_2O_2 dosage was raised from 300 ppm to 1200 ppm,

as a result of the higher hydroxyl radicals production generated by the addition of more peroxide (Eq.1). However, increasing the H_2O_2 concentration beyond 600 ppm led to no significant change in Orange II degradation. Although higher dosages (900 ppm and 1200 ppm) showed faster initial degradation rates, no significant difference in final removal (>95%) was observed after 150 min. At higher peroxide concentrations, scavenging of •OH radicals will occur, which can be expressed by the following equation:

$$H_2O_2 + \bullet OH \rightarrow \bullet HO_2 + H_2O \qquad (Eq.10)$$

Elevated concentrations of peroxide react with •OH radicals to form hydroperoxyl radicals ($\bullet HO_2$), which possess a significantly lower oxidation potential [44, 45]. Consequently, an H_2O_2 dosage of 600 ppm was established as optimal, balancing high catalytic performance and operational cost.

3.3.3 Effect of catalyst dosage

Figure 6.c shows that Orange II degradation occurred most rapidly during the initial 20 min, as the surface active sites of MNP catalyze peroxide decomposition to generate hydroxyl radicals rapidly (Eq.4). Within the first 60 min, dye degradation increased from 30% to 80% when the catalyst concentration was raised from 50 to 75 mg/L, confirming that higher catalyst loading enhances radical production. However, for 100 and 200 mg/L the degradation efficiency decreased. This effect can be attributed to several factors. Firstly, an excess of ferrous species can act as a radical scavenger, competing with Orange II molecules for hydroxyl radicals (Eq.4) and can increase turbidity reducing light penetration consequently, the photoactivation of the catalyst. Secondly, higher nanoparticle concentration promote magnetic agglomeration leading to particle precipitation [46, 47]. Consequently, a catalyst concentration of 75 mg/L was established as optimal for the experimental system.

3.3.4 Effect of initial pH value

pH control plays an important role in dye degradation as it directly influences both hydroxyl radical generation and the availability of iron species in solution. Figure 6.d shows that the degradation efficiency increased as the pH decreased, reaching the highest dye removal at pH 3. After 140 min, approximately 80% degradation was reached at pH 3, whereas degradation efficiency dropped to 55% and 23% at pH 5 and 7, respectively. The drop in dye removal at higher pH values is attributed to the precipitation of ferric ions as insoluble iron hydroxides [48, 49], which reduce the availability of iron species, suppressing the catalytic decomposition of H_2O_2. Consequently, pH 3 was determined as the optimal condition for the evaluated system.

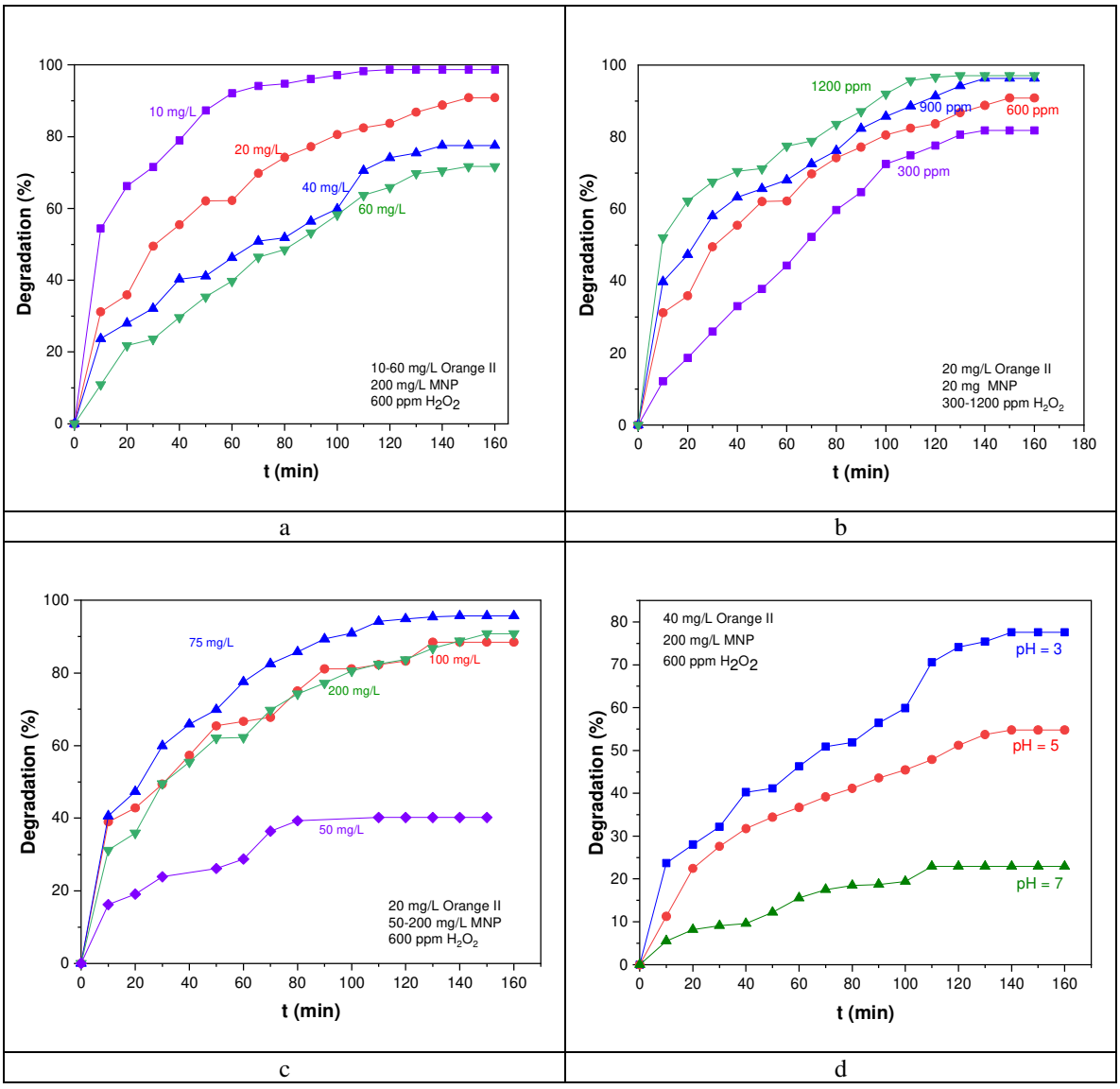


Figure 6. Degradation (%) of Orange II as a function of: a) dye concentration; b) H_2O_2 dosage; c) catalyst dosage; d) initial pH

Table 2 summarizes the experimental conditions and the obtained results.

Table 2. Degradation (%) of Orange II as a function of pH and catalyst, dye and H_2O_2 dosage

	pH	[Orange] (mg/L)	[H_2O_2] (ppm)	[Fe] (mg/L)	Degradation (%)
PHILIPS LAMP –UV LIGHT	3	10	600	200	99
	3	20	600	200	91
	3	40	600	200	78
	3	60	600	200	72
	3	20	300	200	82
	3	20	600	200	91

	3	20	900	200	96
	3	20	1200	200	97
	3	20	600	50	40
	3	20	600	75	96
	3	20	600	100	89
	3	20	600	200	90
	3	40	600	200	78
	5	40	600	200	55
	7	40	600	200	23

Based on the experimental results obtained, the degradation of Orange II using MNP, BMNP and MM as catalyst was compared under specific operating conditions: catalyst concentration 75 mg/L, H_2O_2 600 ppm, dye 40 mg/L and pH 3 (Figure 7). Additionally, MNP was tested as catalyst under solar light irradiation to evaluate its catalytic potential in the photo-Fenton process and the feasibility of operating without an artificial irradiation source. The obtained results are summarized in Table 3.

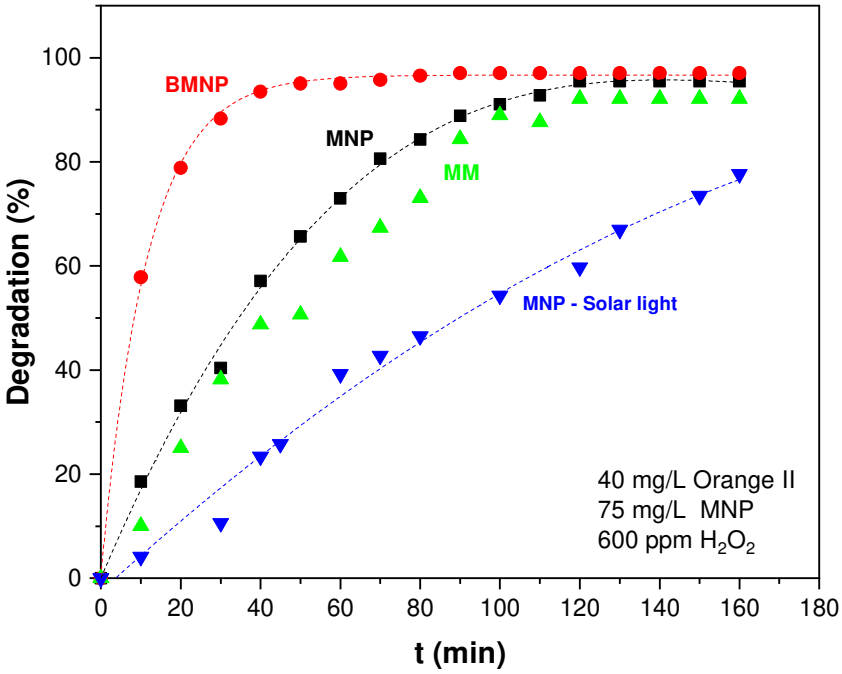


Figure 7. Comparison of Orange II degradation vs. time using MNP, BMNP and MM as catalysts under artificial light and MNP under solar light (Orange II: 40 mg/L; catalyst: 75 mg/L; H_2O_2: 600 ppm; pH = 3)

Table 3. Comparison of Orange II degradation at 160 min under selected conditions

	Sample	pH	[Orange II] (mg/L)	[H_2O_2] (ppm)	[catalyst] (mg/L)	Degradation (%)
PHILIPS LAMP – UV LIGHT	MNP	3	40	600	75	95
	BMNP					97.6
	MM					85
SOLAR LIGHT	MNP					77.7

Based on the degradation profiles shown in Figure 7, the BMNP system demonstrated superior catalytic activity under the proposed operating conditions, achieving the highest degradation efficiency in significantly shorter times. The superior catalytic activity of BMNP compared to MNP and MM can be attributed to a combination of physical and chemical factors. First, the biochar acts as a support that prevents magnetic agglomeration and enhances nanoparticles distribution [50-52]. This exposes a higher density of active catalytic sites leading to a better activation of H_2O_2 while its high adsorption capacity pre-concentrates dye molecules near these active catalytic sites. Furthermore, the increase in the catalyst efficiency may be related to a lower recombination rate between electron/hole pairs (e-/h+) [53, 54], which directly contributes to higher photocatalytic activity. Therefore, this catalyst composed of cobalt ferrite nanoparticles and almond shell biochar emerges as a highly promising material for the photo-Fenton degradation of azo dyes.

Given its superior catalytic efficiency, its degradation performance was evaluated under solar light irradiation with the objective of minimizing operating costs by replacing artificial light sources with solar light. The obtained results are presented in Figure 8.a.

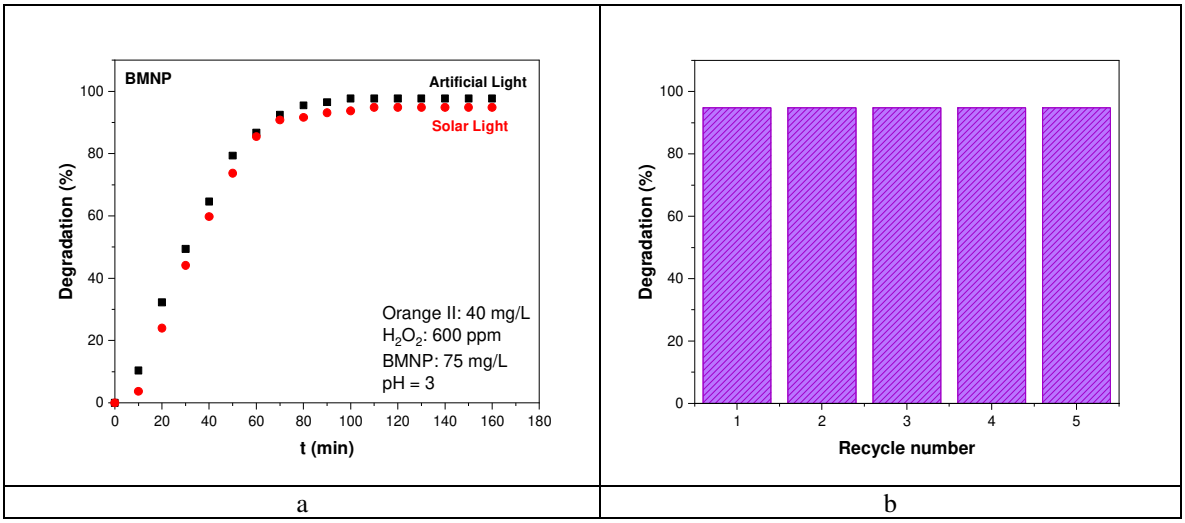


Figure 8. a) Comparison of Orange II degradation vs. time using BMNP as catalyst under artificial light and solar light irradiation; b) Reusability of BMNP (Orange II: 40 mg/L; catalyst: 75 mg/L; H_2O_2: 600 ppm; pH = 3; solar light irradiation)

According to Figure 8.a, BMNP shows comparable catalytic performance under both natural and artificial irradiation sources. In both cases, Orange II removal reached over 95% within 80 min and the degradation

curves exhibit the same kinetic behavior, reaching nearly the same final degradation value. These results confirms the feasibility of replacing artificial light irradiation with natural sunlight irradiation, reducing operational costs without affecting the performance of the photo-Fenton process.

3.4 Catalyst reutilization

In this study, we used BMNP (75 mg/L) as catalyst to degrade a solution of Orange II (40 mg/mL) at pH 3, using 600 ppm of H_2O_2 under solar light irradiation. To investigate whether BMNP particles can be recycled and reused as catalyst in the photo-Fenton process, the materials were regenerated by washing 5 times with water and then sonicated for 5 min, (and 5 times with ethanol and then sonicated for 5 minutes), and dry at room temperature. Noticeably, the catalytic efficiency of the BMNP system was still higher than 94% after been used for five cycles (Figure 8.b).

4. CONCLUSION

Cobalt ferrite magnetic nanoparticles (MNP), cobalt ferrite magnetic nanoparticles synthesized on almond shell biochar (BMNP) and a mechanical mixture of MNP an almond shell biochar (MM) were successfully prepared. The cobalt ferrite presence on biochar and on the mechanical mixture were confirmed by XRD, SEM, magnetic characterization and FTIR, presenting the three samples distinctive characteristics.

Under optimized operating conditions (dye concentration of 40 mg/L, 600 ppm of H_2O_2 and 75 mg/L of catalyst), the BMNP showed superior catalytic performance, reaching approximately 98% dye degradation in significantly shorter times. This enhancement is attributed to the biochar matrix, which reduces magnetic nanoparticle aggregation and suppresses electron/hole recombination. Particularly, identical degradation was observed under artificial and natural sunlight irradiation, validating the use of solar energy to reduce operational costs. Furthermore, BMNP reached more than 94% after 5 successive sorption-washing cycles, which demonstrates exceptional stability and reusability. Consequently, this work highlights BMNP as a sustainable and viable material for large-scale wastewater remediation using solar energy.

REFERENCES

[1] Singh, P. K., Kumar, U., Kumar, I., Dwivedi, A., Singh, P., Mishra, S., Seth, C. S., Sharma, R. K. (2024). Critical review on toxic contaminants in surface water ecosystem: sources, monitoring, and its impact on human health. Environ. Sci. Pollut. Res., 31, 56428-56462. https://doi.org/10.1007/s11356-024-34932-0

[2] Huepa Briñez, J. A., Florez Yepes, G. Y., Hernandez, D. (2024). Causes and effects of contamination of water sources due to excessive use of agrochemicals and pesticides: bibliometric analysis. Water Policy, 26(11), 1086-1102. https://doi.org/10.2166/wp.2024.107

[3] Mmonwuba, N. C., Francis, O. O., Somtochukwu, O., Chinweike, M. P., Ezenwafor, K., Ifunanya, G. E. (2023). Effect of solid waste (leachates) on the quality of underground water. J. Eng Res. Reports, 24(3), 20-31. https://journaljerr.com/index.php/JERR/article/view/805

[4] Kavitha, G., Govindhan, M., Premkumar, S. (2025). Dye pollution and its implications for human health, aquatic ecosystems, and sustainable wastewater treatment: A comprehensive review. J. Water Process Eng., 80, 109071. https://doi.org/10.1016/j.jwpe.2025.109071

[5] Yaseen, D. A., Scholz, M. (2018). Textile dye wastewater characteristics and constituents of synthetic effluents: a critical review. Int. J. Environ. Sci. Technol., 16, 1193-1226. https://doi.org/10.1007/s13762-018-2130-z

[6] Berradi, M., Hsissou, R., Khudhair, M., Assouag, M., Cherkaoui, O., El Bachiri, A., & El Harfi, A. (2019). Textile finishing dyes and their impact on aquatic environs. Heliyon, 5(11). https://doi.org/10.1016/j.heliyon.2019.e02711

[7] Barciela, P., Perez-Vazquez, A., & Prieto, M. A. (2023); Azo dyes in the food industry: Features, classification, toxicity, alternatives, and regulation. Food Chem. Toxicol., 178, 113935. https://doi.org/10.1016/j.fct.2023.113935

[8] Lassoued, A., Liu, L. J., & Li, J. F. (2022). Removal of acid orange II azo dyes using Fe-based metallic glass catalysts by Fenton-like process. J. Mater. Sci., 57(3), 2039-2052. https://doi.org/10.1007/s10853-021-06669-5

[9] Zhang, Y., Shaad, K., Vollmer, D., Ma, C. (2021). Treatment of textile wastewater using advanced oxidation processes - A critical review. Water, 13(24), 3515. https://doi.org/10.3390/w13243515

[10] Ameta, R., Chohadia, A. K., Jain, A., Punjabi, P. B. (2018). Fenton and Photo-Fenton Processes. In Advanced oxidation processes for waste water treatment: Emerging green chemical technology, 49-87. https://doi.org/10.1016/B978-0-12-810499-6.00003-6

[11] Xiao, J., Guo, S., Wang, D., & An, Q. (2024). Fenton-like reaction: recent advances and new trends. Chem. Eur. J., 30(24), e202304337. https://doi.org/10.1002/chem.202304337

[12] AlJaberi, F. Y. (2023). Treatment of refinery wastewater by chemical advanced oxidation processes (UV-photolysis, fenton, and photo-fenton): a comparative study. Iran. J. Chem. Chem. Eng. (Int. Engl. Ed.). https://doi.org/10.30492/IJCCE.2023.560200.5520

[13] Dong, Y., Chen, J., Li, C., & Zhu, H. (2007). Decoloration of three azo dyes in water by photocatalysis of Fe (III)–oxalate complexes/H2O2 in the presence of inorganic salts. Dyes Pigm., 73(2), 261-268. https://doi.org/10.1016/j.dyepig.2005.12.007

[14] Lei, Y., Wang, J., Jiang, B., Liu, H., Lan, H., Zhang, Y., & Gao, G. (2024). Enhanced photo-Fenton degradation of contaminants in a wide pH range via synergistic interaction between 1T and 2H MoS2 and copolymer tea polyphenols/polypyrrole. J. Colloid Interface Sci., 658, 74-89. https://doi.org/10.1016/j.jcis.2023.11.176

[15] Papadopoulou, G., Evgenidou, E., & Lambropoulou, D. (2025). Homogeneous and Heterogeneous Photo-Fenton-Based Photocatalytic Techniques for the Degradation of Nile Blue Dye. Appl. Sci., 15(14), 7917. https://doi.org/10.3390/app15147917

[16] Cao, J., Li, J., Yang, B., Chen, Z., Mahjoub, A. R., & Xing, M. (2024). Gambling of homogeneous and heterogeneous Fenton in wastewater treatment. Cell Rep. Phys. Sci., 5(5). https://doi.org/10.1016/j.xcrp.2024.101966

[17] Soufi, A., Hajjaoui, H., Boumya, W., Elmouwahidi, A., Baillón-García, E., Abdennouri, M., Barka, N. (2024). Recent trends in magnetic spinel ferrites and their composites as heterogeneous Fenton-like catalysts: A review. J. Environ. Manag., 367, 121971. https://doi.org/10.1016/j.jenvman.2024.121971

[18] Khan, A., Valicsek, Z., Horváth, O., Khan, M. M., Wafi, A. (2024). Ferrite-based photocatalysts: Synthesis, modifications, and key parameters in photocatalytic-related applications. Mater. Today Commun., 40, 109556. https://doi.org/10.1016/j.mtcomm.2024.109556

[19] Sayeh, K., Louroubi, A., Abdallah, N., Fkhar, L., Aflak, N., Bahsis, L., ... & El Firdoussi, L. (2025). Elaboration and characterization of Zn1− xCoxFe2O4 spinel ferrites magnetic material: application as heterogeneous catalysts in styrene oxidation. React. Kinet., Mech. Cat., 138(2), 911-927. https://doi.org/10.1007/s11144-024-02763-2

[20] Aldaghri, O. (2025). Efficient photocatalytic degradation of Indigo carmine dye by CoFe2O4@ g-C3N4 nanocomposite. J. Sci.: Adv. Mater. Devices, 100988. https://doi.org/10.1016/j.jsamd.2025.100988

[21] Dharani, S., Gnanasekaran, L., Arunachalam, S., Zielińska-Jure, A., Almoallim, H. S., & Soto-Moscoso, M. (2024). Photodegrading rhodamine B dye with cobalt ferrite-graphitic carbon nitride (CoFe2O4/g-C3N4) composite. Environ. Res., 258, 119484. https://doi.org/10.1016/j.envres.2024.119484

[22] Tamilchezhiyan, M., Begum, A. N., Parthibavarman, M., & Aravindan, S. (2025). Ultra-fast photocatalytic degradation phenomena of methylene blue dye by CoFe2O4 decorated with rGO nanocomposites under visible light irradiation. Diam. Relat. Mat., 151, 111817. https://doi.org/10.1016/j.diamond.2024.111817

[23] Wang, X., Guo, Z., Hu, Z., & Zhang, J. (2020). Recent advances in biochar application for water and wastewater treatment: a review. PeerJ, 8, e9164. https://doi.org/10.7717/peerj.9164

[24] Gwenzi, W., Chaukura, N., Noubactep, C., Mukome, F. N. (2017). Biochar-based water treatment systems as a potential low-cost and sustainable technology for clean water provision. J. Environ. Manag., 197, 732-749. https://doi.org/10.1016/j.jenvman.2017.03.087

[25] Wang, Y., Chen, L., Zhu, Y., Fang, W., Tan, Y., He, Z., & Liao, H. (2024). Research status, trends, and mechanisms of biochar adsorption for wastewater treatment: a scientometric review. Environ. Sci. Eur., 36(1), 25. https://doi.org/10.1186/s12302-024-00859-z

[26] Shaheen, S. M., Niazi, N. K., Hassan, N. E. E., Bibi, I., Wang, H., Tsang, D. C. W., Ok, Y. S., Bolan, N., Rinklebe, J. (2019). Wood-based biochar for the removal of potentially toxic elements in water and wastewater: a critical review. Int. Mater. Rev. 64:216–247. https://doi.org/10.1080/09506608.2018.1473096

[27] Zabaleta, R., Sanchez, E., Fabani, P., Mazza, G., & Rodriguez, R. (2024). Almond shell biochar: characterization and application in soilless cultivation of Eruca sativa. Biomass Convers. Biorefin., 14(15), 18183-18200.c. https://doi.org/10.1007/s13399-023-04002-5

[28] Sachse, E., Escobar-Castillo, M., Waag, F., Gökce, B., Salamon, S., Landers, J., ... & Lupascu, D. C. (2022). Laser ablation of NiFe2O4 and CoFe2O4 nanoparticles. Nanomaterials, 12(11), 1872. https://doi.org/10.3390/nano12111872

[29] Wu, Z., Wang, X., Yao, J., Zhan, S., Li, H., Zhang, J., & Qiu, Z. (2021). Synthesis of polyethyleneimine modified CoFe2O4-loaded porous biochar for selective adsorption properties towards dyes and exploration of interaction mechanisms. Sep. Purifi. Technol., 277, 119474. https://doi.org/10.1016/j.seppur.2021.119474

[30] Shabelskaya, N., Egorova, M., Radjabov, A., Burachevskaya, M., Lobzenko, I., Minkina, T., & Sushkova, S. (2022). Formation of biochar nanocomposite materials based on CoFe2O4 for purification of aqueous solutions from chromium compounds (VI). Water, 15(1), 93. https://doi.org/10.3390/w15010093

[31] Pourreza, N., & Zareian, M. (2009). Determination of Orange II in food samples after cloud point extraction using mixed micelles. J. Hazard. Mater., 165(1-3), 1124-1127. https://doi.org/10.1016/j.jhazmat.2008.10.132

[32] Long, X., Feng, C., Ding, D., Chen, N., Yang, S., Chen, H., ... & Chen, R. (2021). Oxygen vacancies-enriched CoFe2O4 for peroxymonosulfate activation: The reactivity between radical-nonradical coupling way and bisphenol A. J. Hazard. Mater., , 418, 126357. https://doi.org/10.1016/j.jhazmat.2021.126357

[33] El Mashad, H. M., Edalati, A., Zhang, R., & Jenkins, B. M. (2022). Production and characterization of biochar from almond shells. Clean Technol., 4(3), 854-864. https://doi.org/10.3390/cleantechnol4030053

[34] Ribeiro, J. J. K., Porto, P. S. S., Proveti, J. R. C., Pessoa, M. S., Morais, P. C., Moscon, P. S., ... & Muniz, E. P. (2023). Influence of orange residue content on Sol-gel synthesis of cobalt ferrite Nanoparticles: Morphological and magnetic properties. J. Magn. Magn. Mater., 586, 171220. https://doi.org/10.1016/j.jmmm.2023.171220

[35] Sanpo, N., Berndt, C. C., Wen, C., & Wang, J. (2013). Transition metal-substituted cobalt ferrite nanoparticles for biomedical applications. Acta Biomater., 9(3), 5830-5837. https://doi.org/10.1016/j.actbio.2012.10.037

[36] Akbarzadeh, A., Samiei, M., & Davaran, S. (2012). Magnetic nanoparticles: preparation, physical properties, and applications in biomedicine. Nanoscale Res. Lett., 7(1), 144. https://doi.org/10.1186/1556-276X-7-144

[37] Raghavender, A. T. (2013). Synthesis and characterization of cobalt ferrite nanoparticles. Sci. Technol. Arts Res. J., 2(4), 01-04. http://dx.doi.org/10.4314/star.v2i4.1

[38] Ahmad, M., Rajapaksha, A. U., Lim, J. E., Zhang, M., Bolan, N., Mohan, D., ... & Ok, Y. S. (2014). Biochar as a sorbent for contaminant management in soil and water: a review. Chemosphere, 99, 19-33. https://doi.org/10.1016/j.chemosphere.2013.10.071

[39] Nikolić, K., Kragović, M., Stojmenović, M., Popović, J., Krstić, J., Kovač, J., & Gulicovski, J. (2025). Sustainable Carbon Source from Almond Shell Waste: Synthesis, Characterization, and Electrochemical Properties. Materials, 19(1), 8. https://doi.org/10.3390/ma19010008

[40] Maaz, K., Mumtaz, A., Hasanain, S. K., & Ceylan, A. (2007). Synthesis and magnetic properties of cobalt ferrite (CoFe2O4) nanoparticles prepared by wet chemical route. J. Magn. Magn. Mater., 308(2), 289-295. https://doi.org/10.1016/j.jmmm.2006.06.003

[41] Yi, Y., Huang, Z., Lu, B., Xian, J., Tsang, E. P., Cheng, W., ... & Fang, Z. (2020). Magnetic biochar for environmental remediation: A review. Bioresour. Technol., 298, 122468. https://doi.org/10.1016/j.biortech.2019.122468

[42] Rache, M. L., García, A. R., Zea, H. R., Silva, A. M., Madeira, L. M., & Ramírez, J. H. (2014). Azo-dye orange II degradation by the heterogeneous Fenton-like process using a zeolite Y-Fe catalyst—kinetics with a model based on the Fermi's equation. Applied Catalysis B: Environmental, 146, 192-200. https://doi.org/10.1016/j.apcatb.2013.04.028

[43] Guo, J., & Al-Dahhan, M. (2003). Catalytic wet oxidation of phenol by hydrogen peroxide over pillared clay catalyst. Ind. Eng. Chem. Res., 42(12), 2450-2460. https://doi.org/10.1021/ie020344t

[44] Feng, J., Hu, X., Yue, P. L., Zhu, H. Y., & Lu, G. Q. (2003). Discoloration and mineralization of Reactive Red HE-3B by heterogeneous photo-Fenton reaction. Water Res., 37(15), 3776-3784. https://doi.org/10.1016/S0043-1354(03)00268-9

[45] Muruganandham, M., & Swaminathan, M. (2006). Advanced oxidative decolourisation of Reactive Yellow 14 azo dye by UV/TiO2, UV/H2O2, UV/H2O2/Fe2+ processes—a comparative study. Sep. Purif. Technol., 48(3), 297-303. https://doi.org/10.1016/j.seppur.2005.07.036

[46] Nour, M. M., Nabwey, H. A., & Tony, M. A. (2026). Solar-Assisted Hydroxyl Radical-Driven Photo-Fenton-like Catalytic Oxidation of Reactive Azo Dye Using an Iron-Based Metal–Organic Framework. Catalysts, 16(6), 495. https://doi.org/10.3390/catal16060495

[47] Liu, H., Li, G., Qu, J., & Liu, H. (2007). Degradation of azo dye Acid Orange 7 in water by Fe0/granular activated carbon system in the presence of ultrasound. J. Hazard. Mater., 144(1-2), 180-186. https://doi.org/10.1016/j.jhazmat.2006.10.009

[48] Neamtu, M., Yediler, A., Siminiceanu, I., & Kettrup, A. (2003). Oxidation of commercial reactive azo dye aqueous solutions by the photo-Fenton and Fenton-like processes. J. Photochem. Photobiol. Chem. A: Chemistry, 161(1), 87-93. https://doi.org/10.1016/S1010-6030(03)00270-3

[49] Modirshahla, N., Behnajady, M. A., & Ghanbary, F. (2007). Decolorization and mineralization of CI Acid Yellow 23 by Fenton and photo-Fenton processes. Dyes Pigm., 73(3), 305-310. https://doi.org/10.1016/j.dyepig.2006.01.002

[50] Lai, C., Huang, F., Zeng, G., Huang, D., Qin, L., Cheng, M., ... & Chen, L. (2019). Fabrication of novel magnetic MnFe2O4/bio-char composite and heterogeneous photo-Fenton degradation of tetracycline in near neutral pH. Chemosphere, 224, 910-921. https://doi.org/10.1016/j.chemosphere.2019.02.193

[51] Cheng, Z., Li, S., Nguyen, T. T., Gao, X., Luo, S., & Guo, M. (2021). Biochar loaded on MnFe2O4 as Fenton catalyst for Rhodamine B removal: Characterizations, catalytic performance, process optimization and mechanism. Colloids and Surfaces A: Physicochemical and Engineering Aspects, 631, 127651. https://doi.org/10.1016/j.colsurfa.2021.127651

[52] Leichtweis, J., Fuhr, A. C. F. P., Luiz Dotto, G., Mérida, L. G. R., Carissimi, E., Ulbricht, M., & Da Silva, S. W. (2026). MgFe2O4/Biochar Composites for Visible-Light Photo-Fenton Treatment of Azo Dyes: Material

Optimization Assisted by Decision Tree Analysis. Water Air Soil Pollut., 237(18), 1055. https://doi.org/10.1007/s11270-026-09746-0

[53] Leichtweis, J., Ferreira Piazzi Fuhr, A. C., Welter, N., Ramírez Mérida, L. G., & Carissimi, E. (2026). Photo-Fenton process for the degradation of methyl orange, methylene blue and tartrazine present in wastewater using a green composite based on chitin biochar and ZnFe2O4. Waste Biomass Valoriz., 17(1), 187-199. https://doi.org/10.1007/s12649-025-03114-5

[54] Gao, D., Gao, X., Wang, S., Wu, W., Wang, A., Wang, J., & Yao, W. (2024). BNQDs and Fe2O3QDs co-doped in porous g-C3N4 for accelerating photogenerated electron migration and enhancing photo-Fenton catalysis efficiency. J. Environ. Chem. Eng., 12(3), 112781. https://doi.org/10.1016/j.jece.2024.1127